Energy Storage Materials 16 (2019) 632–645

Contents lists available at ScienceDirect

Energy Storage Materials

journal homepage: www.elsevier.com/locate/ensm

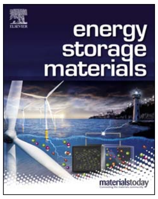

Design and understanding of dendritic mixed-metal hydroxide nanosheets@N-doped carbon nanotube array electrode for high-performance asymmetric supercapacitors

Qiaobao Zhang[a,b], Zaichun Liu[c], Bote Zhao[b], Yong Cheng[a], Lei Zhang[b], Hong-Hui Wu[f], Ming-Sheng Wang[a,*], Shuge Dai[e], Kaili Zhang[d], Dong Ding[b], Yuping Wu[c,*], Meilin Liu[b,*]

[a] *Department of Materials Science and Engineering, College of Materials, Xiamen University, Xiamen, Fujian 361005, China*
[b] *School of Materials Science and Engineering, Georgia Institute of Technology, Atlanta, GA 30332-0245, USA*
[c] *State Key Laboratory of Materials-oriented Chemical Engineering, and School of Energy Science and Engineering, and Institute for Advanced Materials, Nanjing Tech University, Nanjing 211816, China*
[d] *Department of Mechanical and Biomedical Engineering, City University of Hong Kong, 83 Tat Chee Avenue, Hong Kong*
[e] *School of Physical Engineering, Zhengzhou University, Zhengzhou, Henan 450052, China*
[f] *Department of Chemistry, University of Nebraska-Lincoln, Lincoln, NE 68588, United States*

ARTICLE INFO

Keywords:
ZnNiCo carbonate hydroxides
Core/shell nanotube arrays
Hierarchical porous architecture
Asymmetric supercapacitors

ABSTRACT

Design and fabrication of supercapacitors (SCs) with high energy density, fast discharge rate, and long cycle life is of great importance; however, the performances of SCs depend critically on advances in materials development. Here we report the development of a high-performance electrode material composed of hierarchical, porous interlaced ultrathin Zn and Ni co-substituted Co carbonate hydroxides (ZnNiCo-CHs) nanosheets branched on N-doped carbon nanotube arrays (C@ZnNiCo-CHs), which were grown directly on a nickel foam current collector. The mesoporous features and large open spaces of the interlaced ultrathin ZnNiCo-CHs nanosheets provide more active sites for redox reactions and facilitate fast mass transport; the self-standing N-doped carbon nanotube arrays offer large surface area, promote fast electron transport, and enhance structure stability, resulting in outstanding rate capability and long-term stability. Density functional theory calculations suggest that the ZnNiCo-CHs nanosheets have low deprotonation energy, greatly facilitating the rate of redox reactions. Further, an asymmetric SC constructed from a C@ZnNiCo-CHs positive electrode and an N-, S-codoped rGOs negative electrode demonstrates a high energy density of 70.9 W h kg^{-1} at a power density of 966 W kg^{-1} while maintaining a capacity retention of 91% even after 20,000 cycles at 20 A g^{-1}. The findings provide some important insight into rational design of transition metal compounds based materials for fast energy storage, which may be applicable to creating efficient and robust electrode materials for other energy-related devices.

1. Introduction

The ever-increasing environmental pollution and energy crisis have stimulated an intense world-wide interest in the development of high-performance alternative energy storage devices [1–4]. Because of fast discharge rate, long lifespan, and excellent safety, supercapacitors (SCs), also known as electrochemical capacitors, are considered promising energy storage devices. They are potential candidates for extensive applications in high-power electronic devices, emergency power supplies, and hybrid electric vehicles, etc. [5–13]. The performance of SCs depends sensitively on the properties of electrode materials [10,14–16]. Hence various materials have been investigated as the electrodes for SCs, including carbon-based materials, conducting polymers, and various transition-metal oxides, hydroxides, and other compounds [2,3,6,17–23]. Wherein, carbon-based materials have relatively low specific and volumetric capacitances, which severely limit their practical applications [7,24–26]. In contrast, transition-metal hydroxides/oxides, and other compounds can offer much higher specific capacitances and energy densities for their multiple oxidation states, making them attractive candidates for high-performance SCs [18–20,27–29]. In particular, transition-metal (Co, Ni, etc.) hydroxides are promising electrodes for SCs because they possess desirable electrochemical activity and better accessibility to active species [9,19,30]. Unfortunately, the low electronic conductivity of these

---

* Corresponding authors.
E-mail addresses: mswang@xmu.edu.cn (M.-S. Wang), wuyp@fudan.edu.cn (Y. Wu), meilin.liu@mse.gatech.edu (M. Liu).

https://doi.org/10.1016/j.ensm.2018.06.026
Received 20 March 2018; Received in revised form 5 June 2018; Accepted 25 June 2018

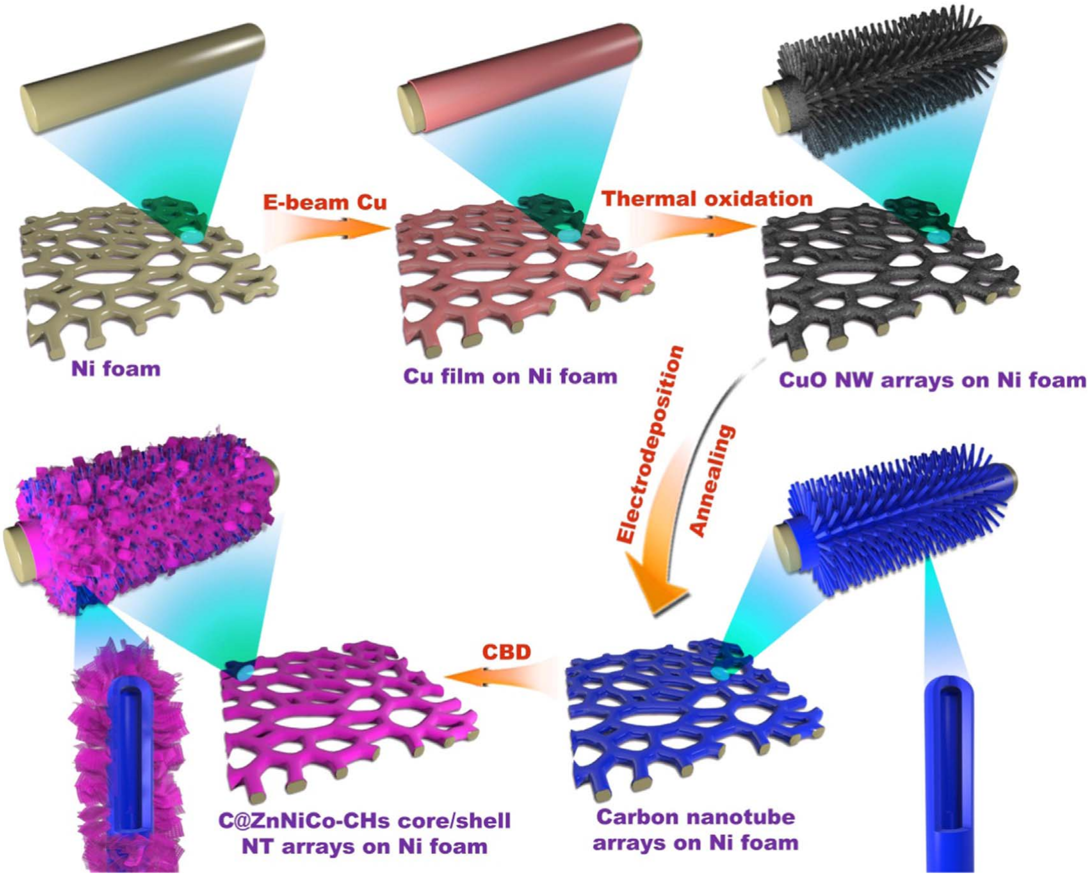

Fig. 1. Schematic illustration of the formation process of hierarchical 3D branched carbon@ZnNiCo CHs core/shell heterostructured nanotube arrays on Ni foam.

hydroxides results in unsatisfactory performance [29,31–33]. Proper combination of these hydroxides with one-dimensional (1D) conductive nanotube arrays on a conductive substrate (current collector) to assemble a hierarchical, three-dimensional (3D) branched core/shell heterostructured arrays is an effective strategy to overcome the aforementioned drawbacks [9,34–38]. Such an electrode may dramatically enhance the electrochemical performance of SCs because of large surface area, direct electronic/ionic transport pathways, synergistic effect and full utilization of electroactive materials [9,35,36,38,39]. Additionally, the direct attachment and close contact of heterostructured nanotube arrays on the current collector ensure good mechanical adhesion and electrical connection [9,27]. Accordingly, tremendous efforts have been devoted to synthesize the self-supported 3D branched heterostructured arrays to improve their electrochemical performances [9,10,27,31,35,36,38,40]. Despite these advances, rational design and fabrication of intriguing 3D branched core/shell heterostructured arrays with simple fabrication methods to achieve distinguished performance are still very challenging.

Recently, incorporating different metal cations into the host to form mixed transition-metal hydroxides has been emerging as an effective way to enhance the electrochemical performance of SCs [41–45]. However, the mechanism of performance enhancement and the role of cation substitution remain largely unknown. Therefore, identifying the underlying mechanism for improved electrochemical performance and seeking ways to optimize the core–shell configuration through smart hybridization are highly desired. Here we present a simple and cost-effective chemical bath deposition (CBD) process for directly fabricating the porous Zn, Ni co-substituted Co carbonate hydroxides (ZnNiCo-CHs) nanosheets on N-doped carbon nanotubes arrays over Ni foam. The resulting electrodes were then used as electrodes for high-performance SCs free from any binders or conductive additives. In our design, N-doped carbon nanotubes arrays are used as backbone, which have better electronic conductivity and stability than the commonly used metal oxides/sulfides nanowires backbone [9,46–49]. Thus, the new electrode architecture allows significantly improved electron transport within every ZnNiCo-CHs nanosheet and throughout the electrode. Further, the increased compositional complexity and potential synergetic effects of the multi-metal components in ZnNiCo-CHs may offer more redox active sites and higher conductivity than the corresponding mono-metal and binary-metal hydroxides, thus enhancing electrochemical performance [16,50]. This electrode configuration offers several fascinating advantages, e.g., large interfacial area for fast electron and ion diffusion, efficient contact between electrolyte ion and active electrode materials for interfacial faradaic reactions, and direct 1D pathway for electron and ion. Accordingly, these electrodes exhibit significantly enhanced electrochemical performance with high specific capacity ($964\,C\,g^{-1}/1928\,F\,g^{-1}$ at $1\,A\,g^{-1}$), outstanding rate capability ($700\,C\,g^{-1}/1400\,F\,g^{-1}$ at $50\,A\,g^{-1}$), and excellent cycling stability (maintained ~96% of the initial capacity after 10,000 cycles at $20\,A\,g^{-1}$), much superior to those electrodes consisting of bare ZnNiCo-CHs nanosheets and the electrodes made of C@Co-CHs, C@ZnCo-CHs, and C@NiCo CHs. The superior performance of our electrodes is attributed mainly to the lower deprotonation energy and easier electron transfer, as evidenced by theoretical calculations. We used N, S- codoped rGOs as the negative electrode because they have higher capacitance and rate capability than the commonly used conventional activated carbon negative electrode [51]. In addition, the N and S dopants in rGOs could offer synergistic effects of the two heteroatoms [52]. As a consequence, an asymmetric SC based on a self-supported C@ZnNiCo-CHs positive electrode and an N, S-codoped rGOs negative electrode demonstrated a high energy density of $70.9\,W\,h\,kg^{-1}$ at a power density of $966\,W\,kg^{-1}$ and capacity retention of 91% even after 20,000 cycles at $20\,A\,g^{-1}$.

2. Results and discussion

The formation process of the hierarchical porous 3D branched C@ ZnNiCo-CHs core/shell heterostructured arrays on Ni foam by a simple CBD method is schematically illustrated in Fig. 1. First, large-scale high-density CuO NW arrays grown vertically on Ni foam were obtained by a simple thermal oxidation of e-beam evaporated Cu film on Ni foam. The growth mechanism responsible for the formation of CuO NW is based on the stress-driven grain-boundary diffusion associated with surface diffusion of Cu atoms/ions [53–55]. Second, the well-aligned N-doped carbon nanotube arrays were obtained by electrodeposition of PPy layer on the CuO NW arrays and a subsequent annealing in N_2 atmosphere at 300 °C for 2 h, which were then used as the scaffold for ZnNiCo-CHs nanosheets growth. The carbon nanotubes were formed by evaporation of the CuO NW cores during heating, as revealed by in-situ TEM observation (Supplementary Fig. S1 and its corresponding video 1). Detailed mechanism of the disappearance of the CuO NW cores at such a low temperature is still under study. Subsequently, the facile and high-efficiency CBD process induced the formation of ZnNiCo-CHs nanosheets on the surface of carbon nanotube arrays backbone, forming 3D hierarchical branched core/shell heterostructured nanotube arrays configuration. It is noteworthy that these ZnNiCo-CHs nanosheets are highly porous, as confirmed by N_2 adsorption-desorption isotherm measurements and TEM analysis.

Supplementary material related to this article can be found online at doi:10.1016/j.ensm.2018.06.026.

In order to determine the crystal structure of the ZnNiCo CHs nanosheets, powder samples collected from the reacted solution by centrifugation were characterized using XRD (Fig. 2a). All diffraction peaks correspond to those for orthorhombic cobalt-based CHs (PDF# 048-0083), suggesting that the partial replacement of cobalt ions by both nickel and zinc ions does not change the crystal structure of cobalt-based CHs [56]. The elemental composition of the ZnNiCo-CHs grown directly on Si substrate was determined by energy dispersive X-ray (EDX) spectroscopy (Fig. 2b); the elements appeared in the spectrum include Zn, Ni, Co, O, C, and Si, with the atomic ratio of Zn/Ni/Co being close to 1:1:2, indicating the formation of pure $(Zn_{0.25}Ni_{0.25}Co_{0.5}\,(OH))(CO_3)_{0.5}$ $\bullet nH_2O$ (while the signal of Si element originates from the silicon substrate). The surface area and pore-size distribution are two key factors that may critically influence the performance of an electrode material for SCs. The surface area and porosity of the ZnNiCo CHs nanosheets were examined using nitrogen isothermal adsorption-desorption measurements (Fig. 2c). As seen in Fig. 2c, a typical IV isotherms with H3-type hysteresis loops ($P/P_0 > 0.4$) was observed, indicating its

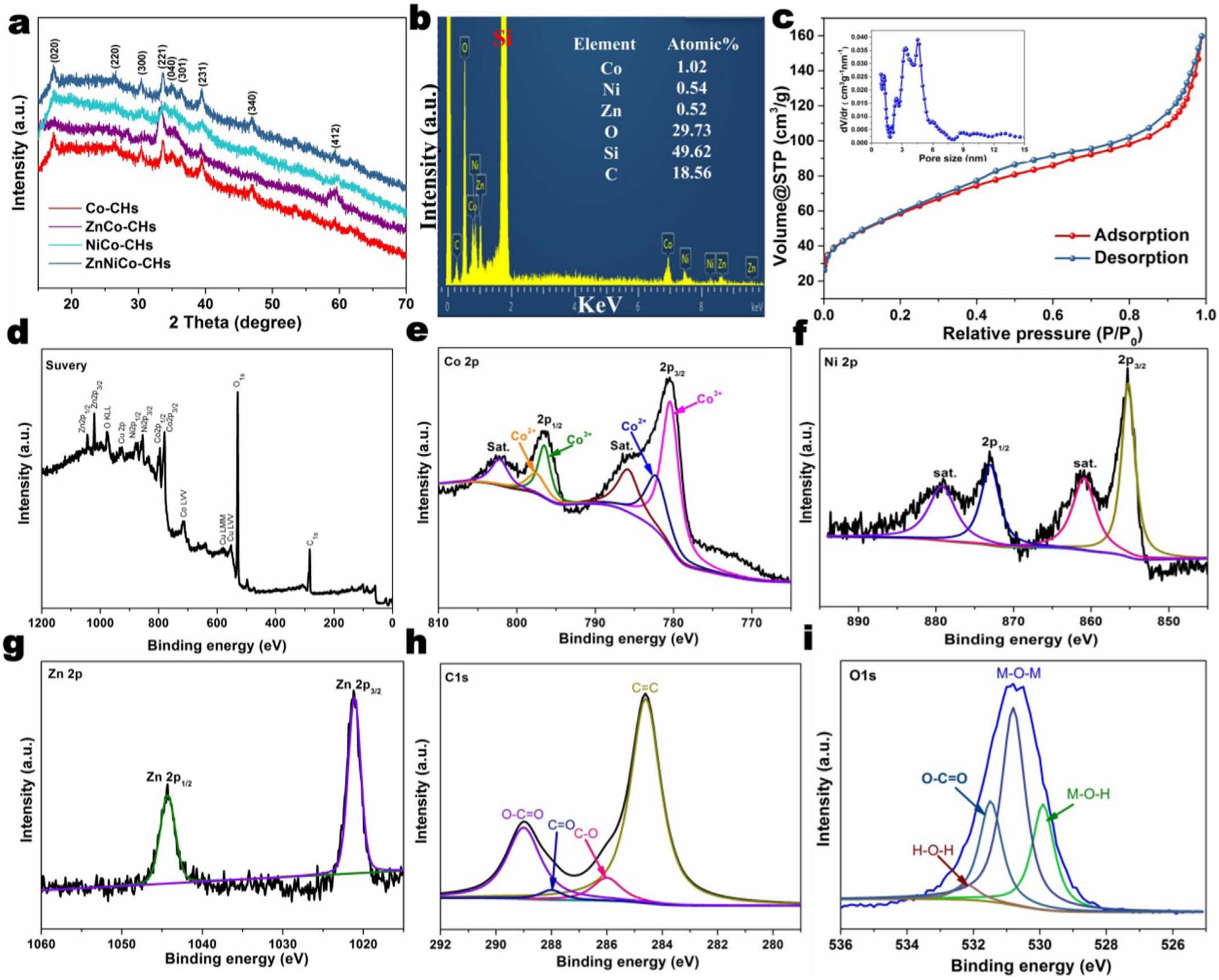

Element	Atomic%
Co	1.02
Ni	0.54
Zn	0.52
O	29.73
Si	49.62
C	18.56

Fig. 2. XRD patterns of (a) Co-CHs , ZnCo-CHs, NiCo-CHs and ZnNiCo-CHs powders, (b) EDX spectrum of ZnNiCo-CHs nanosheets grown directly on Si substrate, (c) the N_2 absorption-desorption isotherm of the as-prepared ZnNiCo CHs nanosheets powders, the inset is the pore distribution, and XPS of (d) survey, (e) high-resolution Co2p, (f) Ni2p, (g) Zn2p, (h) C1s and (i) O1s spectra of C@ZnNiCo-CHs core/shell heterostructured nanotube on Ni foam.

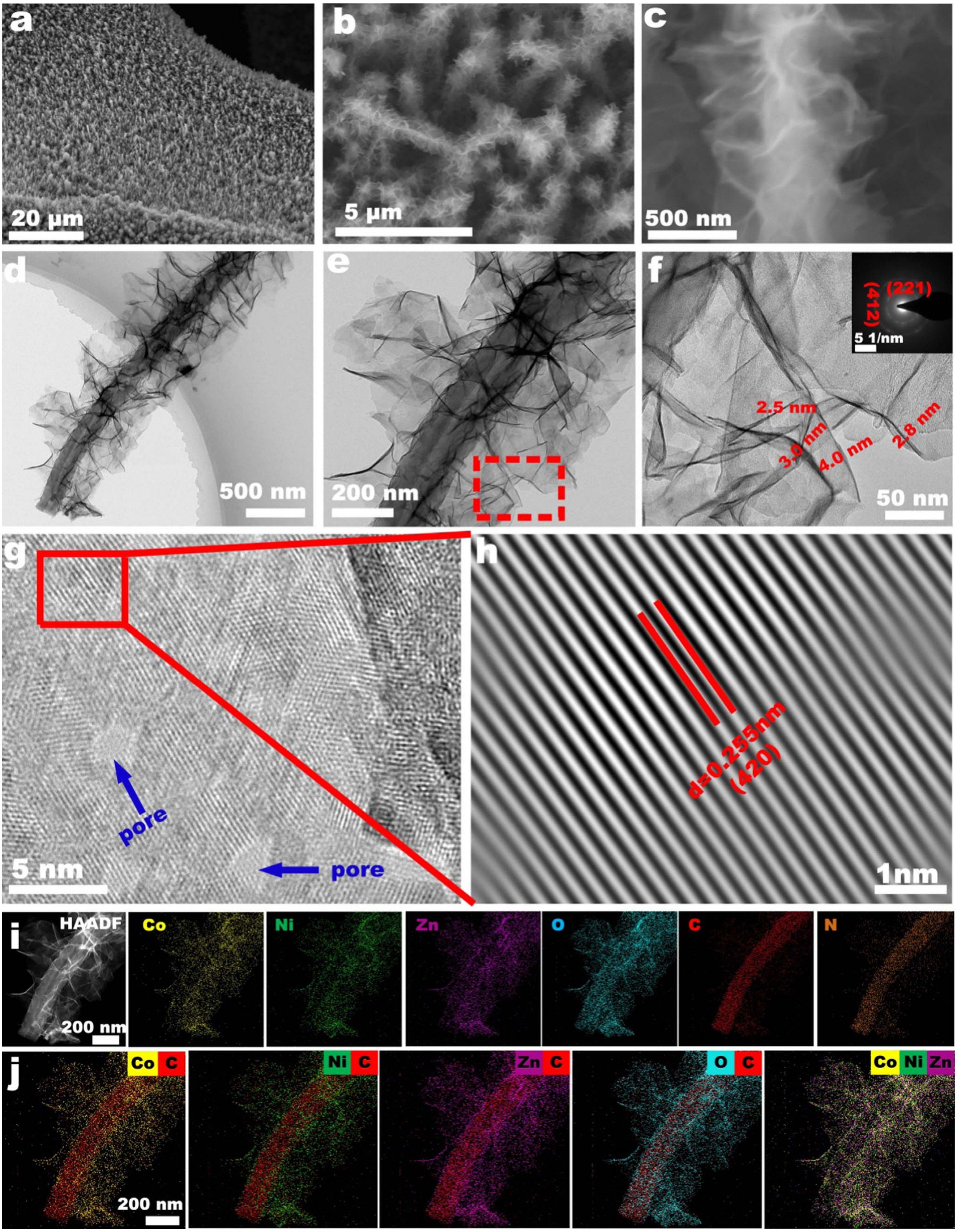

Fig. 3. Typical SEM images of (a–c) hierarchical 3D branched C@ZnNiCo-CHs core/shell heterostructured nanotube arrays on Ni foam, TEM images of (e–d) hierarchical 3D branched C@ZnNiCo-CHs core/shell heterostructured nanotube, inset of (f) is the SAED pattern of ZnNiCo-CHs nanosheets, (e) a closer view of the hierarchical 3D branched C@ZnNiCo-CHs core/shell heterostructured nanotube, (f) a TEM image of branched ZnNiCo-CHs nanosheets taken from the rectangular area marked in (e), (g) HRTEM image of ZnNiCo-CHs nanosheets, (h) enlarged HRTEM image taken from the rectangular area marked in (g) and (i) and (j) STEM images and corresponding Zn,Ni, Co, N, C and O X-ray maps.

mesoporous structures [37]. The pore size distribution, derived from the adsorption data and calculated from the isotherm using the BJH model as shown in the inset of Fig. 2c, suggests that ZnNiCo-CHs nanosheets possess a narrow pore size range of 3–6 nm and an average pore diameter of 4.5 nm and pore volume of 0.209 $cm^3\ g^{-1}$ (Supplementary Table S1). Moreover, the BET specific surface area of ZnNiCo-CHs nanosheets is calculated to be 210.5 $m^2\ g^{-1}$, which is higher than those of Co-CHs, ZnCo-CHs, and NiCo-CHs samples (Supplementary Fig. S2), indicating that the increased surface area may be related to the morphology change, i.e., smaller nanosheets formation caused by Zn and Ni co-substitution. The large specific surface area and unique hierarchical porous structure of ZnNiCo-CHs nanosheets may facilitate good accessibility of the active material to the electrolyte, while the porous structure is beneficial to the kinetics of reaction and the mechanical integrity [7,26]. The surface electronic state and the composition of the C@ZnNiCo-CHs core/shell heterostructured nanotube arrays were analyzed by X-ray photoelectron spectroscopy (XPS) and the corresponding results are presented in Fig. 2d–i. The survey spectrum shown in Fig. 2d indicates the presence of Ni, Co, Zn, Cu, C and O and the absence of other impurities. By using a Gaussian fitting method, the high-resolution Co2p emission spectrum (Fig. 2e) was best fitted with two spin–orbit doublets, which are characteristic of Co^{2+} and Co^{3+}, and two couple of shakeup satellites (identified as "Sat.") [43]. Regarding the high-resolution Ni 2p spectrum (Fig. 2f), it was consists of two spin-orbit doublets at 855.2 eV and 873.1 eV, suggesting the Ni^{2+} oxidation state in ZnNiCo-CHs and two shakeup satellite [42,57]. For high-resolution Zn 2p spectrum (Fig. 2g), two major peaks at 1020.7 and 1043.8 eV are ascribed to Zn $2p_{3/2}$ and Zn $2p_{1/2}$ of Zn(II), respectively [57]. The high-resolution of C 1s peak (Fig. 2h) was further deconvoluted into one dominant peak and three weak peaks assigned to carbon atoms in four different functional groups: non-oxygenated carbon at 284.6 eV, carbon in C-O bond at 285.9 eV, the carbonyl carbon (C=O) at 287.9 eV, and the carboxylate carbon (O-C=O) at 289.0 eV [58].The high-resolution of O1s peak (Fig. 2i) exhibited four different peaks at 530.8, 531.5, 529.9, and 532.2 eV, corresponding to functional groups of

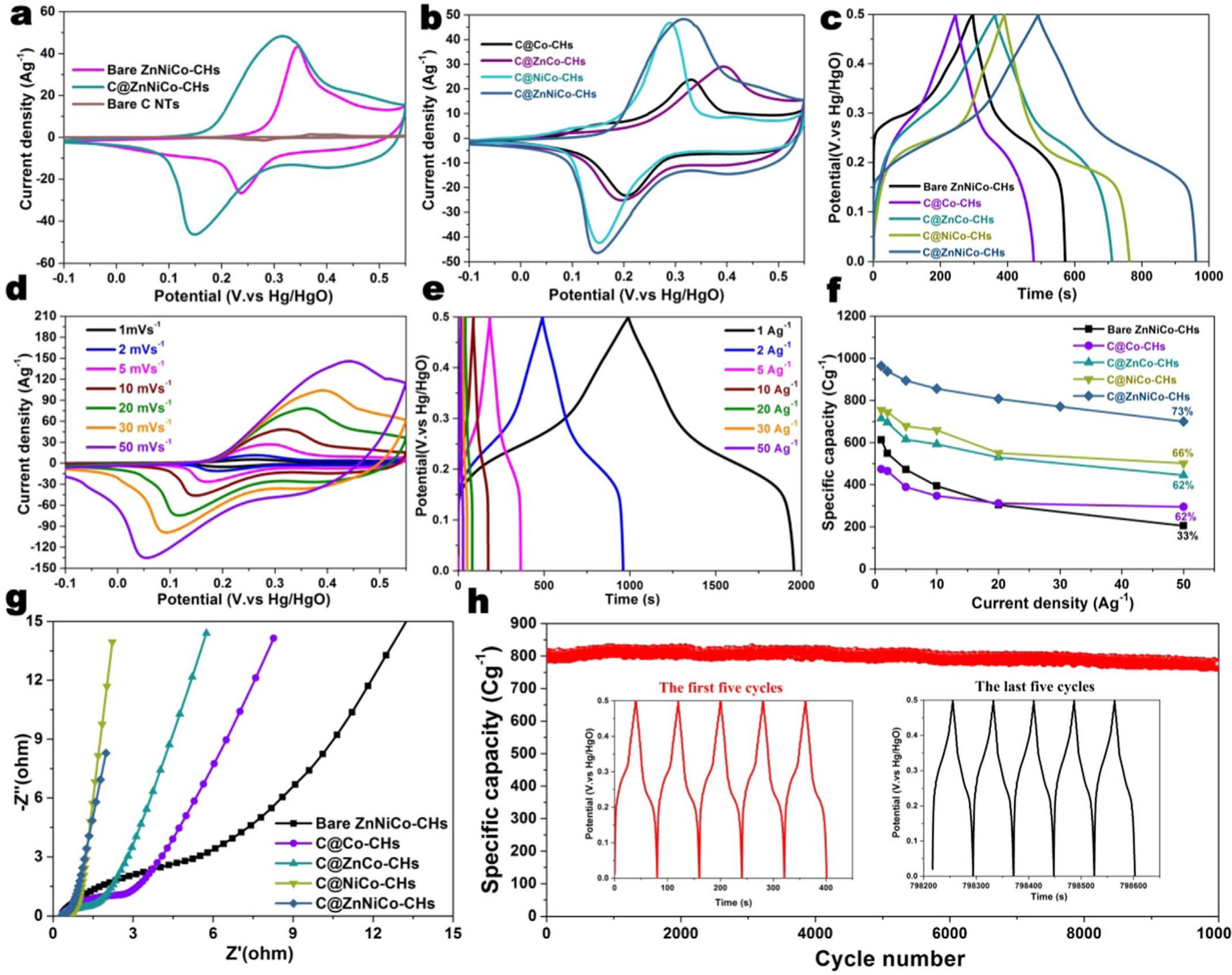

Fig. 4. (a) CV curves of bare C nanotube arrays, ZnNiCo-CHs nanosheets, and C@ZnNiCo-CHs core/shell heterostructured nanotube array electrodes at a scan rate of 10 $mV\ s^{-1}$, (b) CV curves of C@Co-CHs, C@ZnCo-CHs, C@NiCo-CHs and C@ZnNiCo-CHs core/shell heterostructured nanotube array electrodes at a scan rate of 10 $mV\ s^{-1}$, (c) galvanostatic charge/discharge (GCD) curves of bare ZnNiCo-CHs nanosheets, C@Co-CHs, C@ZnCo-CHs, C@NiCo-CHs and C@ZnNiCo-CHs core/shell heterostructured nanotube array electrodes at current density of 2 $A\ g^{-1}$, (d) typical CV curves of C@ZnNiCo-CHs core/shell heterostructured nanotube array electrode at different scan rates, ranging from 1 $mV\ s^{-1}$ to 50 $mV\ s^{-1}$, (e) galvanostatic charge/discharge (GCD) curves of C@ZnNiCo-CHs core/shell heterostructured nanotube array electrode at various current densities, (f) specific capacity of bare ZnNiCo-CHs nanosheets, C@Co-CHs, C@ZnCo-CHs, C@NiCo-CHs and C@ZnNiCo-CHs core/shell heterostructured nanotube array electrodes at different current densities, (g) electrochemical impedance spectra (EIS) of bare ZnNiCo-CHs nanosheets, C@Co-CHs, C@ZnCo-CHs, C@NiCo-CHs and C@ZnNiCo-CHs core/shell heterostructured nanotube array electrodes acquired at open circuit potential and (h) long-term cyclic performance of C@ZnNiCo-CHs core/shell heterostructured nanotube array electrode at a current density of 20 $A\ g^{-1}$, inset is its corresponding GCD curves of the first and last five cycles.

metal–oxygen bonds (M-O-M), metal-carbonates (O-C=O), metal hydroxides (M-O-H), and hydroxyl oxygen (H–O-H), respectively.

Fig. 3 shows some typical microscopic features of the C@ZnNiCo-CHs core/shell heterostructured nanotubes as revealed by SEM, TEM, and HRTEM, while the images of CuO nanowires together with N-doped carbon nanotubes are given in the supplemental information. As shown in supplementary Fig. S3, the obtained CuO nanowires have diameters of ~ 30 nm and length ranging from 5 µm to 10 µm with single-crystalline nature, grown approximately perpendicular to the surface of the substrate to form densely-packed nanowires arrays over a large area with good uniformity. After electrodeposition , it can be clearly seen that a PPy layer is grown uniformly on the surface of CuO NW array and does not degrade the ordered structure, (Supplementary Fig. S4a–c) but increase the diameter of the nanowires. According to the low-resolution TEM image, the PPy shell is homogeneous with a thickness of ~ 30 nm (Supplementary Fig. S4e). The element distribution of a CuO/ PPy NW was further analyzed by energy dispersive X-ray (EDX) spectroscopy mapping (Supplementary Fig. S4g). Evidently, Cu and O are locally confined in the core region, while C and N are distributed over the shell. After annealing, it can be found that the as-obtained top-closed carbon nanotubes uniformly stand on the surface of the Ni foam and they are separate with each other (Supplementary Fig. S5a–c), forming array configuration. The carbon nanotubes with a diameter of ~ 115 nm and wall thickness of ~ 30 nm are amorphous with a very smooth surface (Supplementary Fig. S5d–f). The EDX elemental mapping (Supplementary Fig. 5h) reveals the uniform dispersion of C and N elements throughout the nanotube region. After the growth of ZnNiCo-CHs nanosheets on carbon nanotubes by a CBD process, the surface of the carbon nanotubes is covered by high-density, secondary ZnNiCo-CHs nanosheets (Fig. 3a–b), producing thicker layers and rougher surfaces. Uniform deposition of many ZnNiCo-CHs nanobranches on the surface of carbon nanotubes created 3D branched core/shell heterostructured nanotube arrays, as can be clearly observed in Fig. 3c; the uniform array structure still remained even after the two components were integrated. More interestingly, the void space between neighboring heterostructured nanotube arrays is widely open (Fig. 3b), which is favorable for easy electrolyte penetration so that every nanosheet participates in the electrochemical reaction. It is interesting to observe that the simultaneous incorporation of multi-component of Zn and Ni element into Co-CHs results in a remarkable morphological transformation from nanowires to ultrathin nanosheets (Supplementary Fig. S6). The ultrathin nanosheet morphology has proven to be more favorable for the performance enhancement of SCs [26]. A typical bright field TEM image in Fig. 3d–e clearly shows the core/shell nanotube architecture. Many branched ZnNiCo-CHs nanosheets feature a transparent, folded, silk-like morphology; they appear tightly bonded on the surface of carbon nanotube core (Fig. 3d–e), forming a typical branched core/shell heterostructured configuration. The dark strips in nanosheets are generally the folded edges or wrinkles of the nanosheets [44]. The nanosheet shell (inset of Fig. 3f) shows a polycrystalline SAED pattern corresponding to the cobalt-based CHs phase (PDF# 048-0083) [56]. The magnified TEM image shown in Fig. 3e unambiguously reveals the entire and intimate coating of carbon nanotube core with ZnNiCo-CHs nanosheets shells. Such an intimate interface contact between carbon nanotube and ZnNiCo-CHs branches may be favorable for improving the electrochemical performances. The enlarged TEM image of the nanosheet shell (Fig. 3f) shows that the tip of the dark strip is 2–4 nm in thickness. The HRTEM image (Fig. 3g–h) of the nanosheet shell shows clear fringes with a measured interplanar spacing of 0.26 nm, which correspond to the interplanar distance of the (420) planes of cobalt-based CHs. These branched nanosheets shells are porous but structurally continuous (Fig. 3g), which is consistent with the BET results. It is well known that the mesoporous structures of the nanosheets are important to facilitating mass transport within the electrodes for fast redox reactions and greatly increase the electrode/electrolyte contact area, thus enhancing electrochemical performance [7,44]. The chemical compositions of the carbon core nanotube and the ZnNiCo CHs shell nanosheets were further distinguished using STEM elemental mapping. As seen in Fig. 3i–j, the distributions of Co, Ni, Zn and O are relatively uniform throughout the backbone and the branch region, whereas that of C and N are dominant only in the backbone region, suggesting that the growth of ZnNiCo-CHs shell was on the surface of the carbon nanotube core.

The electrochemical properties of the 3D hierarchical porous branched C@ZnNiCo-CHs core/shell electrodes were characterized in test cells with a three-electrode configuration in a 2 M KOH electrolyte solution at room temperature. Fig. 4a-b shows some typical voltammograms (CV) of bare carbon nanotubes (C NTs), bare ZnNiCo-CHs nanosheets (See SEM and TEM images in Supplementary Fig. S7), C@Co-CHs (SEM images in Supplementary Fig. S6a–b), C@ZnCo-CHs (SEM images in Supplementary Fig. S6c–d), C@NiCo-CHs (SEM images in Supplementary Fig. S6e–f), and C@ZnNiCo-CHs core/shell heterostructured nanotube arrays electrode at a scan rate of 10 mV s^{-1}. It is noted that the bare carbon nanotube and the Ni foam substrate are relatively inactive in the system under the electrochemical testing conditions (Supplementary Fig. S8), suggesting that they make negligible contribution to the capacity of the electrodes; their primary functions are mechanical support and current collection. As for the bare ZnNiCo-CHs nanosheets, C@Co-CHs, C@ZnCo-CHs, C@NiCo-CHs, and C@ZnNiCo-CHs core/shell heterostructured nanotube array electrodes (Fig. 4a–b), a pair of redox peaks can be clearly observed in the potential range of − 0.1 V to 0.5 V, attributed to the faradaic redox reaction related to M-O/MO-OC (M represents Co or Ni, C represents H), an indication of battery-type behavior of the as-obtained electrodes [42,44]. The component zinc was proven to have a minimal role in providing active sites for electrochemical reactions, but has an effect on promoting reaction species in accessing the oxidized cobalt and nickel ions [57,59,60] and thus endowing more efficient faradaic redox reaction process, as suggested by Density functional theory (DFT) calculations. Apparently, the C@ZnNiCo-CHs core/shell heterostructured nanotube array electrode exhibit higher peak current density and larger increment of the CV integrated area in comparison with that of the bare ZnNiCo-CHs nanosheets (Fig. 4a). This indicates that the carbon nanotube array on the surface of the nickel foam plays an essential role in enhancing the SCs performance. Importantly, the C@ZnNiCo-CHs core/shell heterostructured nanowire array electrode demonstrates the largest increment of the CV integrated area in comparison with those of the C@Co-CHs, C@ZnCo-CHs, and C@NiCo-CHs electrodes, indicating the largely enhanced electrochemical reaction activity, which could be attributed to the synergistic effect resulting from the more active sites offered by Zn, Ni co-substituted Co-CHs. Fig. 4c shows the galvanostatic charge/discharge (GCD) curves of the bare ZnNiCo-CHs nanosheets, C@Co-CHs, C@ZnCo-CHs, C@NiCo-CHs, and C@ZnNiCo-CHs core/shell heterostructured nanotube array electrodes at current density of 2 A g^{-1}. Evidently, the C@ZnNiCo-CHs core/shell heterostructured nanotube array electrode delivers the longest discharge time among all electrodes studied, offering the highest specific capacity. The representative CV curves of the C@ZnNiCo-CHs core/shell heterostructured nanotube array electrode at scan rates ranging from 1 to 50 mV s^{-1} are shown in Fig. 4d; The presence of a pair of well-defined redox peaks in all CV curves confirm that the electrochemical capacitance of the C@ZnNiCo-CHs core/shell heterostructured nanotube arrays is derived from battery-type behavior of the material. More interestingly, it is noted that the change in redox current and the change in the shape of the CV curves are insensitive to the increase in the scan rate, suggesting that the unique architecture of C@ZnNiCo-CHs core/shell heterostructured nanotube arrays is favorable for fast redox reactions or high cycling rates. Furthermore, it is evident that the separation between the oxidation and the reduction peak increased with the scan rate, due likely to the Ohmic resistance of the cell.

To further elucidate the feature of the charge storage process of our electrodes, a related analysis can be performed from CV regarding the behavior of the peak current density by assuming the current density, i, obeys a power-law relationship with the sweep rate [61–63]:

$$i = ab^{v} \tag{1}$$

where a is a constant and ν is the sweep rate. The b-value can be determined by the slope of the log(v)–log(i) plots. In particular, the b-value of 0.5 indicates a semi-infinite diffusion behavior, whereas 1.0 represents a capacitive process. The log(v)–log(i) plots for the bare ZnNiCo-CHs, C@Co-CHs, C@ZnCo-CHs, C@NiCo-CHs, and C@ZnNiCo-CHs electrodes is shown in Supplementary Fig. S9. The b-value for both cathodic and anodic peaks of each sample at scan rates from 2 to 20 mV s^{-1} is higher than 0.5, suggesting that the electrochemical behavior of each electrode is attributed to both capacitive and semi-infinite diffusion process [64]. The higher b-value for the electrodes of C@Co-CHs, C@ZnCo-CHs, C@NiCo CHs and C@ZnNiCo-CHs indicates that they exhibit a higher degree of capacitive charge storage compared to that of bare ZnNiCo-CHs/Ni foam electrode, indicating that more capacitive charge storage contribution can be obtained with the introduction of self-supporting N-doped carbon nanotube. The small variation in b-value for the electrodes of C@Co-CHs, C@ZnCo-CHs, C@NiCo CHs and C@ZnNiCo-CHs is due probably to the different morphologies, voltage, and particle sizes of the samples [63,64].

Fig. 4e shows some typical GCD curves of the C@ZnNiCo-CHs core/shell heterostructured nanotube array electrode. These charge and discharge curves are highly symmetric and show a well-defined discharge voltage plateau between 0.25 and 0.1 V, indicating that the hybrid composite has a good electrochemical battery-type characteristic and superior reversible redox reaction [65]. The specific capacities/capacitances of the electrodes, calculated from the discharge curves in Fig. 4e and Supplementary Fig. S10 using Eqs. (2)/(3), are displayed in Fig. 4f. Obviously, the C@ZnNiCo-CHs core/shell hetero-

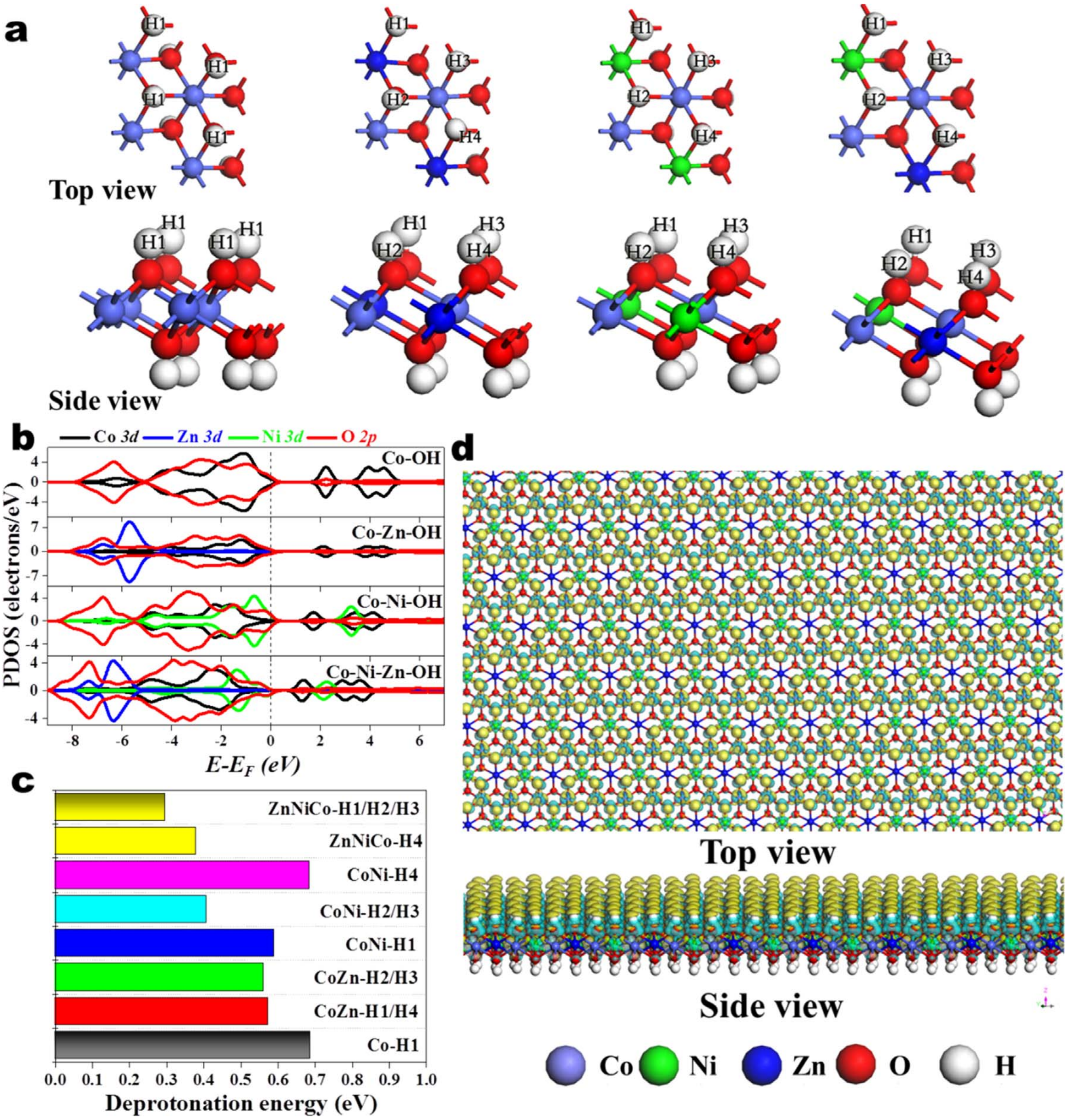

Fig. 5. a) Top and side views for atomic structures of Co hydroxide-based slabs: Co-OH, Co-Zn-OH, Co-Ni-OH, and Co-Ni-Zn-OH. b) Partial density of states calculated for Co, Co-Zn, Co-Ni, and Co-Ni-Zn hydroxide systems; c) the calculated deprotonation energy for the deprotonation process on Co hydroxide-based structure slabs; Co-Ni-Zn-H1 represents deprotonation of H1 site on a Co-Ni-Zn hydroxide structure slab. d) charge density difference isosurfaces for the deprotonation process on Co-Ni-Zn hydroxide; cyan and yellow colors indicate charge depletion and charge accumulation zones, respectively (isosurface value is 0.05 eV/Å^3).

structured nanotube array electrode exhibited specific capacity of 964 C g^{-1} (equivalent to 1928 F g^{-1}) at current density of 1 A g^{-1}, much higher than those of the bare ZnNiCo-CHs nanosheets (613 C g^{-1}/1226 F g^{-1} at 1 A g^{-1}, Supplementary Fig. S10c), C@Co-CHs (474 C g^{-1}/948 F g^{-1} at 1 A g^{-1}, Supplementary Fig. S10f), C@ZnCo-CHs (714 C g^{-1}/1428 F g^{-1} at 1 A g^{-1}, Supplementary Fig. S10i), C@NiCo-CHs (755 C g^{-1}/1510 F g^{-1} at 1 A g^{-1}, Supplementary Fig. S10l) electrodes and other reported self-supported metal hydroxides and 3D metal oxides core/shell heterostructured arrays electrodes (Supplementary Table S2). More remarkable is the high rate capability of the C@ZnNiCo-CHs core/shell nanotube arrays electrode: at 50 A g^{-1} it still retained ~ 73% (700 C g^{-1}/1400 F g^{-1}) of the capacity measured at 1 A g^{-1}; in contrast, the capacity of the bare ZnNiCo-CHs nanosheets electrode at 50 A g^{-1} was only ~ 33% (205 C g^{-1}/410 F g^{-1}) of that at 1 A g^{-1}, similar to other reported metal hydroxides electrodes (Supplementary Table S3). This result further indicates that more efficient current collection and better utilization of the active electrode material in this composite electrode becomes more pronounced at higher cycling rates. The improved electrochemical performance is due probably to a fact that the branched ZnNiCo-CHs nanosheets connected directly with carbon nanotube arrays forming 3D hierarchical branched core/shell heterostructured nanotube arrays. This configuration can enable the full exposure of ZnNiCo-CHs nanosheets to the electrolyte and the carbon nanotube arrays on Ni foam with a large surface area endows an enhanced contact of ZnNiCo-CHs nanosheets with both the electrolyte and current collector, allowing easy electrolyte penetration and every nanosheet participates in the electrochemical reaction [38]. Moreover, the direct attachment and close contact of carbon nanotube arrays on Ni foam is capable of providing a 1D conductive framework of ZnNiCo-CHs nanosheets for fast charge transport, resulting in a short diffusion length and efficient current collection necessary for higher capacity and rate capability [32,38]. Besides the good specific capacity and excellent rate capability, the long-term cyclic stability is another critical issue for practical applications of SCs. Fig. 4h shows the long-term cycling performance of C@ZnNiCo-CHs core/shell heterostructured nanotube array electrode at high current density of 20 A g^{-1} over 10,000 cycles. Even after 10,000 cycles, the specific capacity can retain 96% of the initial value, demonstrating the excellent long-term electrochemical stability. Additionally,the long-term electrochemical stability can be further verified by the very stable charge/discharge curve for the first and last five cycles (inset of Fig. 4h). Further, the electrochemical impedance spectra (EIS) of the electrodes were acquired at open circuit potential (Fig. 4g). Each of the impedance spectrum consists of a semicircle in the high frequency region, which corresponds to the charge transfer resistance at the working electrode/electrolyte interface, and a straight line in the low frequency region, which corresponds to the Warburg impedance (Z_w) or the impedance to mass transfer (such as ion diffusion) associated with the electrode reactions [46,66]. Obviously, the C@Co-CHs, C@ZnCo-CHs, C@NiCo-CHs and C@ZnNiCo-CHs core/shell heterostructured nanotube arrays electrodes had a more ideal straight line (closer to vertical) than that of the bare ZnNiCo-CHs nanosheets electrode, and also exhibit smaller semicircle diameter than that of the bare ZnNiCo-CHs nanosheets electrode, implying the important role of carbon nanotube arrays acting as a superhighway for electron/ion transport in promoting conductivity and charge-transfer. In the high frequency region, the impedances of C@Co-CHs, C@ZnCo-CHs, C@NiCo-CHs and C@ZnNiCo-CHs core/shell heterostructured nanotube arrays electrodes are much smaller than that of the C@Co-CHs electrode, suggesting enhanced charge transfer kinetics of the redox reaction with the favorable Zn and/or Ni-substitution. In particular, C@ZnNiCo-CHs core/shell heterostructured nanotube arrays electrode showed the lowest polarization impedance (i.e., the smallest size of the impedance loop) among all the investigated electrode materials. This result demonstrates that C@ZnNiCo-CHs core/shell heterostructured nanotube arrays on Ni foam is a favorable electrode with enhanced electronic conductivity and charge-transfer at the electrode/electrolyte interface, which is attributed mainly to the facile electron/ion transport of the Zn, Ni co-substituted Co hydroxides and the quick transport of electrons along the carbon nanotubes.

It is well established that Zn partially replace the cobalt species in Co hydroxides/oxides can create more redox active sites and enhance the conductivity, thus effectively improving the electroactivity and supercapacitive properties [57,59,67,68]. Moreover, the increased compositional complexity and potential synergetic effects of the multi-metal components in ZnNiCo-CHs may further enrich the redox centers, which is helpful to obtain high electrochemical activities [16,50,60]. To better understand the chemical composition and potential synergetic effect on the electrochemical reaction mechanism in mixed-transition metal hydroxide, we performed first-principles calculations using a model derived from partial substitution of lattice Co atoms by Ni/Zn atoms in the $Co(OH)_2$ structure (Fig. 5a). Calculated partial density of states (PDOS) (Fig. 5b) and band structure diagrams (Supplementary Fig. S11) clearly show that the outermost orbitals of Co and Ni contribute greatly to the electronic states near the Fermi level. Moreover, both single-metal (Ni- or Zn-) substitution and multi-metal (both Ni and Zn) co-substitution in Co hydroxide diminished the band gap, leading to facile electronic conduction and excitation, in which multi-metal cosubstitution was somewhat better than single-metal substitution. From the PDOS results, we can find out how each system works. Compared to $Co(OH)_2$, both Zn and Ni single atom substitution promoted the redox activities of Co atom. Further, Ni-substitution also obviously increased charge density around the Fermi level (but Zn did not), which makes CoNi-binary hydroxide have a narrower band gap than CoZn-binary hydroxide. A synergistic effect was observed between the three Co/Ni/Zn atoms, making the outermost orbitals electrons of Ni and Co more active and the cosubstituted CoNiZn-ternary system possess the narrowest band gap and the optimal oxidation properties. The electronic conductivity and better oxidation in CoNiZn-ternary was predicted beneficial for the deprotonation performance, which potentially influences the driving force for the charge–discharge process and the electrochemical properties. Our calculated deprotonation energies of $Co(OH)_2$, $Co_{0.5}Zn_{0.5}(OH)_2$, $Co_{0.5}Ni_{0.5}(OH)_2$, and $Co_{0.5}Ni_{0.25}Zn_{0.25}(OH)_2$ confirmed this prediction, as shown in Fig. 5c. The calculated deprotonation energies results are consistent with the oxidation and electronic conductivity analysis. This energy is reduced by Zn or Ni substitution, more so by Zn and Ni cosubstitution (0.31–0.39 eV) due to a synergistic effect of Zn and Ni. Fig. 5d exhibits the color-filled charge density difference isosurfaces for the deprotonation process on the Co-Ni-Zn hydroxide model. The intimate charge interchange occurs mainly between hydrogen atom and Ni/Co through oxygen atom while Zn exhibits barely charge transfer during deprotonation process. In this synergistic system, Zn atom mainly plays the key role of refueling by facilitating the electronic transfer between Co/Ni and O anions. This effect is also validated through the transfer Hirshfeld charges analysis for the deprotonation process as demonstrated in Supplementary Fig. S12 and Table S4. Overall, DFT calculations clearly demonstrated that multi-metal (Ni and Zn) cosubstitution in Co hydroxide significantly enhanced the electron transfer between metal cations (Co/Ni) and O so that facilitated the deprotonation/protonation reaction process, achieving fast kinetics and thus high electrochemical performance. And the theoretical calculation results regarding the effect of multi-metal cosubstitution well matched with the experimental observations. To investigate the advantages of Zn in Co-Ni-Zn hydroxide system, we carefully selected and compared two other metals, Mg and Cd, which have the same oxidation state as Zn. Although the PDOS (Supplementary Fig. S13g) results indicate that a similar synergistic effect is also expected in the Co-Ni-Mg and Co-Ni-Cd hydroxide systems, the Co-Ni-Zn hydroxide system has the highest electronic conductivity with the narrowest band gap of 1.155 eV (Supplementary Fig. S13b) and the lowest minimum deprotonation energy

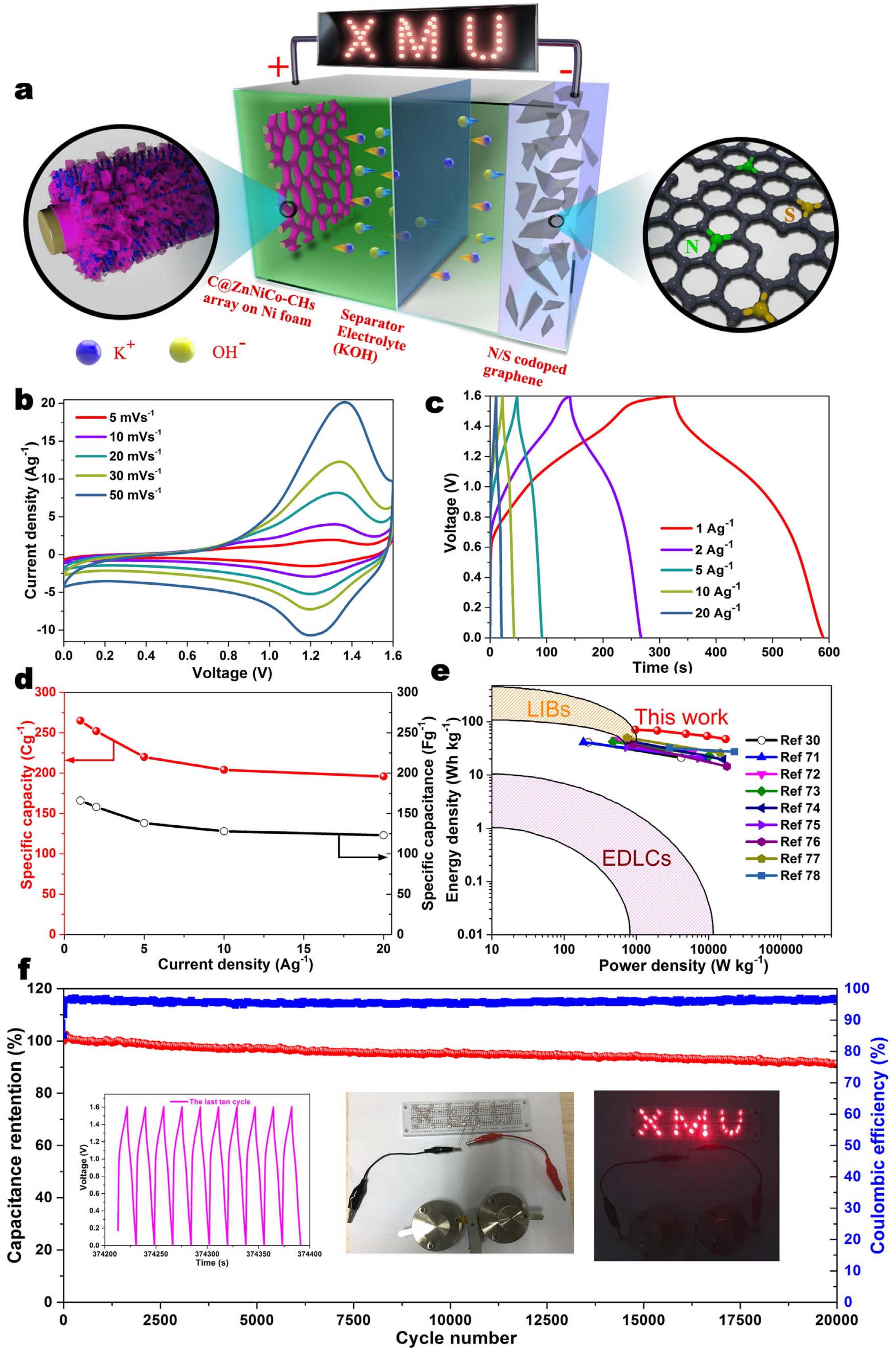

Fig. 6. (a) Schematic illustration of the C@ZnNiCo-CHs //N,S-codoped rGOs asymmetric SC configuration, electrochemical performance of the C@ZnNiCo-CHs //N,S-codoped rGOs asymmetric supercapacitor of (b) cyclic voltammetry curves, (c) galvanostatic charge/discharge curves, (d) cell capacity/capacitance vs current density, (e) Ragone plot (energy density vs power density). (f) cycling stability performance at a current density of 20 A g^{-1}, inset is its corresponding charge/discharge curves of the last ten cycles ; the inset digital photo is a XMU logo consisting of 31 red LEDs in parallel powered by two asymmetric supercapacitor devices in series.

(Supplementary Fig. S13h), suggesting that Zn/Ni co-substituted Co hydroxides is the best candidate for facile electron transfer, rapid redox reaction, and thus high electrochemical performance.

Further, an asymmetric supercapacitor was constructed using a C@ ZnNiCo-CHs CHs based positive electrode and an N, S-codoped rGOs (Supplementary Fig. S14,15) negative electrode, as schematically shown in Fig. 6a. The mass ratio of the positive to the negative electrode was kept at 0.303 (see the detailed mass balance process in Supporting information) according to their individual electrochemical behaviors (Supplementary Fig. S16a) and the optimum operating voltage window was set at 1.6 V (Supplementary Fig. S16b). Shown in Fig. 6b are the CV curves of the asymmetric SC acquired at different scan rates in the potential range of 0–1.6 V in 2 M KOH aqueous electrolyte; a pair of well-defined redox peaks are visible between 0.5–1.6 V in all CV curves, indicating its battery-type behavior. The corresponding galvanostatic charge/discharge curves at different current densities (Fig. 6c) are nonlinear, which is in congruent with the CV results. As seen in Fig. 6d, the specific capacities/capacitances calculated from typical galvanostatic charge/discharge curves at different current densities are 265 C g^{-1} (166 F g^{-1}), 252 C g^{-1} (158 F g^{-1}), 220 C g^{-1} (138 F g^{-1}), 204 C g^{-1} (128 F g^{-1}), and 196 C g^{-1} (123 F g^{-1}), respectively, at current densities of 1, 2, 5, 10, 20 A g^{-1} (based on the total mass of active materials from both positive and negative electrodes). As seen in the Ragone plot (Fig. 6e), the asymmetric device delivered an energy density of 70.9 W h kg^{-1} at a power density of 966 W kg^{-1}. Moreover, an energy density of 47.4 W h kg^{-1} can still be retained at a power density of 17.25 kW kg^{-1} (equivalent to a discharge time of 9.9 s), demonstrating its ultrafast energy storage capability. In particular, the asymmetric SC delivered much higher energy density than the EDLCs at the same power density, much higher power density than the LIBs at the same energy density, comparable energy densities to those of the LIBs at the same power density [69,70]. Furthermore, the gravimetric energy and power densities of the asymmetric SC were superior to many systems reported previously, including α-(Ni/Co)$(OH)_2$/graphene//AC [30], Co-Al hydroxide/dodecyl sulfate anions/G//sandwiched G/porous C [71], G@NiO-1//NGH [72], $NiCo_2S_4$/N-doped carbon (C) foam//ordered mesoporous C/N-doped C foam [73], $NiCo_2S_4$ ball-in-ball hollow spheres//graphene/carbon spheres [74], CNT@$Ni(OH)_2$//3DGN, NiCo hydroxides/G/Ni foam//AC [75], $CoMoO_4$//AC [76], C cloth@$NiCo_2O_4$//C cloth@nitrogen-doped C flakes [77] and NiO-porous C hollow sphere//N-doped G [78]. The cycling performance of the C@ZnNiCo-CHs //N,S co-doped rGOs asymmetric SC was measured at a high current density of 20 A g^{-1} up to 20,000 cycles (Fig. 6f). Impressively, ~ 91% of its initial capacitance was maintained after 20,000 cycles, which outperformed the reported results of advanced hybrid/asymmetric supercapacitors as shown in Supplementary Table S5, illustrating the excellent long-term electrochemical stability of the hybrid SC device, as confirmed by the corresponding GCD curves in the inset of Fig. 6f. Moreover, a simple application of the asymmetric SC was also demonstrated; a XMU

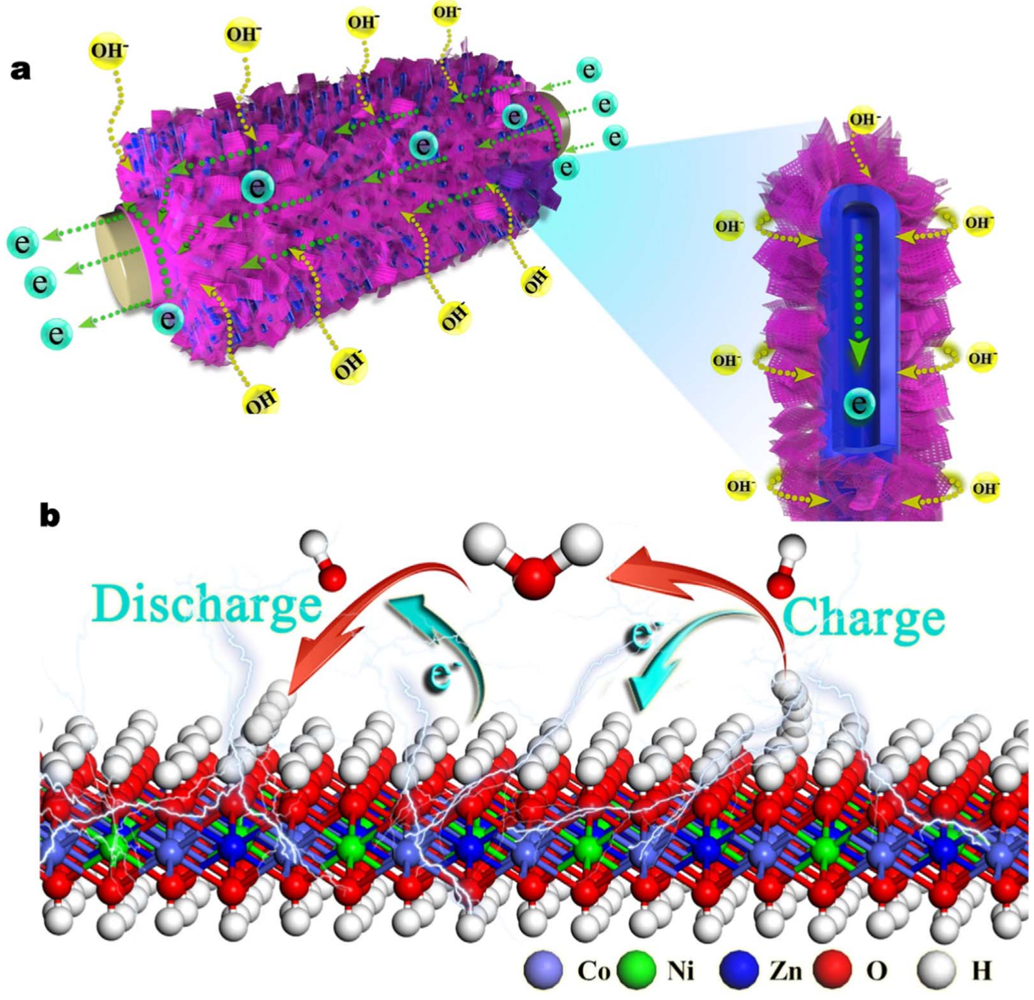

Fig. 7. (**a**) Schematic illustrations of the electron and ion transport pathways in self-supported C@ZnNiCo-CHs CHs core/shell heterostructured nanotube arrays electrode and its enlarged one with individual C@ZnNiCo-CHs CHs core/shell heterostructured nanotube (on right) and (b) Schematic illustrations of the deprotonation/protonation reaction process of atomically thin 2D ZnNiCo-CHs CHs nanosheet electrode.

(Xiamen University) logo consisting of 31 red LEDs in parallel was powered by two asymmetric SC devices in series after being charged to 3.2 V (inset in Fig. 6f), demonstrating its viability and potential in practical applications (for detailed information, see corresponding video 2 in supplemental information).

Supplementary material related to this article can be found online at doi:10.1016/j.ensm.2018.06.026.

The excellent electrochemical performance of the C@ZnNiCo-CHs based electrode is attributed mainly to the following structural features and electrode architectures. First, the direct growth of N-doped carbon nanotube arrays on a 3D Ni foam not only serves a large surface area enabling more reaction sites of ZnNiCo-CHs nanosheets, which is favorable for ZnNiCo-CHs nanosheets accessible to an electrolyte, but also provides 1D transport pathway for efficient current collection (Fig. 7a). Second, the hierarchical porous configuration with abundant void space enables the full exposure of the ZnNiCo-CHs nanosheets to the electrolyte and ensures every ZnNiCo-CHs nanosheet participates in the electrochemical reactions and enhances the structural stability during ion intercalation, while the ultrathin thickness facilitates fast diffusion of ions due to short diffusion length, resulting in high capacitance and outstanding rate capability (Fig. 7a). Third, the direct attachment and close contact of C@ZnNiCo-CHs core/shell heterostructured nanotube arrays on a highly conductive Ni foam substrate could ensure good mechanical adhesion and minimal interfacial resistance, important to outstanding rate capability (Fig. 7a). In addition, the atomically thin 2D nanosheets enable complete hydrogen atom exposure on the surface and the Zn and Ni co-substituted Co carbonate hydroxides make the deprotonation more easily, which provide much more chance for hydrogen desorption and hence efficiently facilitate the Faradaic redox reactions, accounting for higher capacity and superior rate capability (Fig. 7b) [79,80].

3. Conclusion

In summary, hierarchical, porous 3D branched core/shell heterostructured N-doped carbon nanotube arrays coated with ZnNiCo-CHs nanosheets have been successfully designed and fabricated. In this electrode architecture, the well-aligned N-doped carbon nanotube arrays grown directly on Ni foam not only serve as a high-surface-area scaffold to increase the exposure of the ZnNiCo-CHs nanosheets but also allow fast electron conduction and ion diffusion, thus accelerating the rate of faradaic redox reactions. The DFT-based calculations reveal that the Zn and Ni co-substituted Co carbonate hydroxides can reduce the deprotonation energy and facilitate the electron transport that is responsible for the enhanced electrochemical performance. When tested as an electrode (without the addition of any binders or conductive additives) in a SC, the core/shell heterostructured nanotube arrays displayed significantly enhanced electrochemical performance, demonstrating high specific capacity (964 C g^{-1}/1928 F g^{-1} at 1 A g^{-1}), outstanding rate capability (700 C g^{-1}/1400 F g^{-1} at 50 A g^{-1}), and excellent cycling stability (retained ~ 96% of the initial capacitance after 10,000 cycles at 20 A g^{-1}). These performances are far better than those of a bare ZnNiCo-CHs nanosheets electrode. More importantly, the asymmetric SC delivers superior energy densities of 70.9 and 47.4 W h kg^{-1} at power densities of 966 W kg^{-1} and 17.25 kW kg^{-1} (discharge time of 9.9 s), respectively, while maintaining a long cycle-life of 20,000 cycles at 20 A g^{-1}. Further, the developed protocol to construct hierarchical, porous 3D branched core/shell heterostructured nanotube arrays with dramatically enhanced charge and mass transport may be applicable to other hybrid materials for a wide range of applications.

4. Experimental section

4.1. Materials synthesis

CuO nanowire arrays grown on Ni foam were fabricated by simple thermal oxidation of e-beam evaporated Cu film on Ni foam. Commercially available nickel foam (Changsha Lyrun New Materials Co. Ltd.) was used as the conductive substrate. The nickel foam was ultrasonically cleaned in alcohol for 10 min, adequately rinsed with alcohol and distilled water, and blow-dried by compressed air. The nickel foam was then placed inside a conventional electron beam evaporation system (JunSun EBS-500). After the vacuum level in the chamber reached 1.6×10^{-6} Torr, a layer of copper with thickness of 3 μm was deposited onto the nickel foam by e-beam evaporation. The nickel foam with a Cu film was heated in a furnace for 12 h at 400 °C in static air to grow CuO nanowires. The furnace was then naturally cooled to room temperature.

The N-doped carbon nanotube arrays on Ni foam were obtained by the electrodeposition of PPy layer on CuO NW arrays followed with annealing in N_2 atmosphere. First, the as-obtained CuO nanowire arrays on nickel foam were used as the scaffold for the growth of PPy shell by potentiostatic deposition. 0.34 g pyrrole (100 mM), 0.43 g $LiClO_4$ (80 mM) and 1.63 g (112 mM) sodium dodecyl sulfate (SDS) were dissolved in 100 ml of deionized water to obtain the electrolyte for electropolymerization of PPy. The electropolymerization of PPy was carried out with a CHI 660E electrochemical workstation using a three-electrode configuration, in which the as-synthesized CuO nanowire array electrode, Ag/AgCl and a Pt foil were used as the working electrode, reference electrode and counter electrode, respectively. The coaxial CuO@PPy core–shell nanowire arrays on Ni foam were synthesized potentiostatically at 0.8 V for 10 s. The N-doped carbon nanotube arrays grown directly on Ni foam was then obtained by annealing the as-prepared coaxial CuO@PPy core–shell nanowire arrays on Ni foam in Ar atmosphere at 300 °C for 2 h.

Hierarchical 3D branched C@ZnNiCo-CHs core/shell heterostructured nanotube arrays on Ni foam were synthesized by chemical bath deposition (CBD). In a typical procedure, the as-obtained N-carbon nanotube arrays on Ni foam were immersed into a closed 600 mL Pyrex beaker with 400 mL aqueous solution, containing 27.83 g of urea, 1.19 g (0.01 M) zinc nitrate hexahydrate, 4.65 g (0.04 M) nickel(II) nitrate hexahydrate and11.64 g (0.1 M) cobalt(II) nitrate hexahydrate and the beaker containing the growth solution and substrates was then covered with an aluminum foil and placed in an oven maintained at 85 °C for 2 h. After the beaker naturally cooled down to room temperature, the substrates were then taken out of the solution and cleaned in distilled water by ultrasonic for several times and finally dried at 80 °C for 6 h to obtain hierarchical 3D branched C@ZnNiCo-CHs core/shell heterostructured nanotube arrays on Ni foam.

A hydrothermal method was used to prepare the N,S-codoped graphene (N, S-codoped rGOs). Typically, 25 ml of the GO aqueous (2 mg/ml) was dispersed in 25 mL of deionized water and mixed with 0.76 mg thiourea under magnetically stirring for 0.5 h. The mixture was reacted in a Teflon-lined stainless steel autoclave at 180 °C for 12 h. After being washed repeatedly with deionized water several times to remove the residual thiourea, the he black hydrogel was freeze-dried to obtain the N, S-codoped rGOs.

4.2. Sample characterization

The morphology, crystalline structure, and composition of the as-grown samples were characterized using field emission scanning electron microscopy (Hitachi S4800 FESEM), transmission electron microscopy (FEI Talso 200 s), and X-ray diffraction (XRD) analysis (PW-1800 system). In Situ TEM imaging was carried out on a FEI Talso 200 s/200 kV TEM. The in situ heating studies were conducted using a Protochips Aduro heating holder. NW samples for the heating tests were prepared by drop-casting liquid suspensions onto Aduro thermal devices and then allowed to fully air-dry before further use. All heating steps were conducted at the rate of 10 °C ms^{-1} to gradually increase the temperature.

4.3. Electrochemical performance evaluation

The electrochemical measurements such as cyclic voltammetry (CV), galvanostatic charge/discharge, and electrochemical impedance spectroscopy (EIS) were performed on CHI 660E (Chenhua, Shanghai) electrochemistry workstation using a three-electrode cell whereas the long-term cycling performance was evaluated using an LAND-CT2001A battery testing instrument. In a typical electrochemical test, 1 cm^2 of the as-prepared C@ZnNiCo-CHs core/shell heterostructured nanotube arrays on Ni foam (without any polymer binder or conductive additives) was used as the working electrode, a Pt plate (facing to the working electrode) and Hg/HgO as the counter and the reference electrode, respectively, in a freshly prepared 2 M KOH aqueous electrolyte. The distance between the working electrode and the counter electrode was about 1 cm. The potential range for the CV measurements was between – 0.1 and 0.55 V vs. Hg/HgO at scan rates ranging from 1 to 50 $mV\,s^{-1}$. The galvanostatic charge/discharge tests were conducted in a stable potential window between 0 and 0.5 V at different current densities. EIS measurements were carried out by applying an AC voltage with 5 mV amplitude in a frequency range from 0.01 Hz to 100 kHz at open circuit potential. At the beginning of each electrochemical measurement, the working electrode (or cell) was activated via cyclic voltammetry test at a scan rate of 30 $mV\,s^{-1}$ for 10–20 cycles until cyclic voltammograms became relatively stable. The long-term cycling performance of the three-electrode or two-electrode cells was recorded after the initial activation process. The mass loading of active ZnNiCo-CHs on the carbon nanotube/Ni foam substrate was about 1.8 $mg\,cm^{-2}$ and the bare ZnNiCo-CHs on Ni foam was around 1.5 $mg\,cm^{-2}$. The mass loading was determined from the difference in weight of the carbon nantoube arrays on a Ni foam substrate as measured using a microbalance (Mettler Toledo XS3DU with an accuracy of 1 μg) before and after the CBD deposition. The specific capacity Q ($C\,g^{-1}$) of the battery-type electrodes was calculated as follows [81]:

$$Q(Cg^{-1}) = i_m{*}\Delta t \tag{2}$$

where i_m = I/m ($A\,g^{-1}$) is the current density, I is the current, m (g) is the mass of the active electrode material and Δt (s) is the discharge time. For easier understanding and comparison with reported results, the specific capacitance Q ($F\,g^{-1}$) of our electrode was calculated as follows:

$$Q(Fg^{-1}) = \frac{I\Delta t}{m\Delta U} \tag{3}$$

where I is current (A), Δt (s) is the discharge time, ΔV (V) is the potential window, and m (g) is mass of active materials.

The N, S-codoped rGOs negative electrode was prepared as follows: the N/S codoped graphene materials was ground and sieved through a 170-mesh sieve before using; a mixture slurry containing of 90 wt% active materials, and 10 wt% PTFE binder was well prepared in ethanol and then rolled with the assistance of ethanol to form a uniform free-standing film. For testing in a three-electrode configuration, the working electrode was obtained by pressing the free-standing film between two nickel foams. For asymmetric supercapacitor device, the self-supporting C@ZnNiCo-CHs grown directly on Ni foam was used as positive electrode; a freestanding film of N,S-codoped rGOs materials with one piece Ni foam above that was used as current collectors by only physical contact as negative electrode. A 2 M KOH aqueous solution was used as electrolyte, and a NKK separator (MPF30AC-100, Nippon Kodoshi Corporation, Kochi, Japan) was used as the separator. The electrodes were soaked in the electrolyte solution for approximately 1 h under vacuum and were assembled in a split test cell (MTI Corporation) under ambient atmosphere. The cell was finally tightened by 4 nuts and bolts before the electrochemical measurement. The specific capacitance Q ($F\,g^{-1}$) of asymmetric supercapacitors is calculated based on Eq. (3). The energy density ($W\,h\,kg^{-1}$) of the asymmetric supercapacitor device was calculated from the galvanostatic discharge curve using the following equation [69,82]:

$$E = I\int Vdt/3.6(mC@ZnNiCo - CHs + mN, S - codoped\ rGOs) \tag{4}$$

The constant 3.6 is adopted when the energy density (E) is in $W\,h\,kg^{-1}$, the current (I).

is in mA, the voltage (V) is in V, the time (t) is in seconds, and the mass (m) is in mg. The mass used in the calculation for asymmetric SC device was based on the total mass of C@ZnNiCo-CHs composite and N,S-codoped rGOs.

The power density P ($W\,kg^{-1}$) was calculated using the following equation:

$$P = E/\Delta t \tag{5}$$

4.4. Density functional theory calculations

DFT-based first-principles calculations were performed with the generalized gradient approximation (GGA) [83] in the form of PW91 [84], as implemented in the CASTEP package [85] of Materials Studio. The final set of energies for all calculations was computed with an energy cut off of 780 eV. Geometry optimization was performed using a 2a × 2b × 1c supercell single layer with 20 Å vacuum space to avoid the interaction form nearby layers. All atoms were fully relaxed until the residual forces on each atom became smaller than 0.03 meV $Å^{-1}$, and the convergence criteria for energy were set to be 10^{-5} eV. The Brillouin zone integration was performed with 3 × 3 × 1 Γ-centred Monkhorst-Pack k-point meshes in geometry optimization. The deroprotonation energy is defined as: $E_{deprotonation} = E_{defect} - E_{perfect}+0.5E_{H_2}$

Acknowledgments

This work was supported by the National Natural Science Foundation of China (Grants nos. 21703185, 51425301 and U1601214), The Fundamental Research Funds for the Central Universities (Xiamen University: 20720170042), Guangdong Innovative and Entrepreneurial Research Team Program (No. 2014ZT05N200), and the US National Science Foundation (DMR-1410320 and DMR-1742828). The computational resources generously provided by the High Performance Computing Center of Nanjing Tech University are greatly appreciated. Q. Z and Z. L. contributed equally to this work.

Appendix A. Supplementary material

Supplementary data associated with this article can be found in the online version at doi:10.1016/j.ensm.2018.06.026.

References

[1] P. Simon, Y. Gogotsi, Materials for electrochemical capacitors, Nat. Mater. 7 (2008) 845.
[2] G. Wang, L. Zhang, J. Zhang, A review of electrode materials for electrochemical supercapacitors, Chem. Soc. Rev. 41 (2012) 797–828.
[3] Y. Wang, Y. Song, Y. Xia, Electrochemical capacitors: mechanism, materials, systems, characterization and applications, Chem. Soc. Rev. 45 (2016) 5925–5950.
[4] P. Simon, Y. Gogotsi, B. Dunn, Where do batteries end and supercapacitors begin?, Science 343 (2014) 1210–1211.
[5] J. Yan, Q. Wang, T. Wei, Z. Fan, Recent advances in design and fabrication of electrochemical supercapacitors with high energy densities, Adv. Energy Mater. 4 (2014) 1300816.
[6] J. Liu, J. Wang, C. Xu, H. Jiang, C. Li, L. Zhang, J. Lin, Z.X. Shen, Advanced energy storage devices: basic principles, analytical methods, and rational materials design, Adv. Sci. (2017) 1700322.
[7] G. Zhang, X.W. Lou, General solution growth of mesoporous $NiCo_2O_4$ nanosheets on various conductive substrates as high-performance electrodes for supercapacitors, Adv. Mater. 25 (2013) 976–979.
[8] J. Liu, J. Jiang, C. Cheng, H. Li, J. Zhang, H. Gong, H.J. Fan, Co_3O_4 Nanowire@ MnO_2 ultrathin nanosheet core/shell arrays: a new class of high-performance pseudocapacitive materials, Adv. Mater. 23 (2011) 2076–2081.

[9] J.A. Syed, J. Ma, B. Zhu, S. Tang, X. Meng, Hierarchical multicomponent electrode with interlaced Ni(OH)$_2$ nanoflakes wrapped zinc cobalt sulfide nanotube arrays for sustainable high-performance supercapacitors, Adv. Energy Mater. 7 (2017) 1701228.

[10] G. Zhang, T. Wang, X. Yu, H. Zhang, H. Duan, B. Lu, Nanoforest of hierarchical Co$_3$O$_4$@NiCo$_2$O$_4$ nanowire arrays for high-performance supercapacitors, Nano Energy 2 (2013) 586–594.

[11] W. Zuo, C. Xie, P. Xu, Y. Li, J. Liu, A novel phase-transformation activation process toward Ni-Mn-O nanoprism arrays for 2.4 V ultrahigh-voltage aqueous supercapacitors, Adv. Mater. 29 (2017).

[12] N. Jabeen, A. Hussain, Q. Xia, S. Sun, J. Zhu, H. Xia, High-performance 2.6 V aqueous asymmetric supercapacitors based on in situ formed Na0.5 MnO2 nanosheet assembled nanowall arrays, Adv. Mater. 29 (2017).

[13] R. Li, Y. Wang, C. Zhou, C. Wang, X. Ba, Y. Li, X. Huang, J. Liu, Carbon-stabilized high-capacity ferroferric oxide nanorod array for flexible solid-state alkaline battery-supercapacitor hybrid device with high environmental suitability, Adv. Funct. Mater. 25 (2015) 5384–5394.

[14] M.R. Lukatskaya, B. Dunn, Y. Gogotsi, Multidimensional materials and device architectures for future hybrid energy storage, Nat. Commun. 7 (2016) 12647.

[15] Y. Cheng, H. Zhang, C.V. Varanasi, J. Liu, Improving the performance of cobalt–nickel hydroxide-based self-supporting electrodes for supercapacitors using accumulative approaches, Energy Environ. Sci. 6 (2013) 3314.

[16] C. Yuan, H.B. Wu, Y. Xie, X.W. Lou, Mixed transition-metal oxides: design, synthesis, and energy-related applications, Angew. Chem. 53 (2014) 1488–1504.

[17] W. Zuo, R. Li, C. Zhou, Y. Li, J. Xia, J. Liu, Battery-supercapacitor hybrid devices: recent progress and future prospects, Adv. Sci. 4 (2017) 1600539.

[18] G. Zhang, X. Xiao, B. Li, P. Gu, H. Xue, H. Pang, Transition metal oxides with one-dimensional/one-dimensional-analogue nanostructures for advanced supercapacitors, J. Mater. Chem. A 5 (2017) 8155–8186.

[19] X. Li, D. Du, Y. Zhang, W. Xing, Q. Xue, Z. Yan, Layered double hydroxides toward high-performance supercapacitors, J. Mater. Chem. A 5 (2017) 15460–15485.

[20] X. Li, A.M. Elshahawy, C. Guan, J. Wang, Metal phosphides and phosphates-based electrodes for electrochemical supercapacitors, Small 13 (2017).

[21] Y. Liu, Y. Li, H. Kang, T. Jin, L. Jiao, Design, synthesis, and energy-related applications of metal sulfides, Mater. Horiz. 3 (2016) 402–421.

[22] X.-Y. Yu, L. Yu, X.W.D. Lou, Metal sulfide hollow nanostructures for electrochemical energy storage, Adv. Energy Mater. 6 (2016) 1501333.

[23] T. Zhai, S. Sun, X. Liu, C. Liang, G. Wang, H. Xia, Achieving insertion-like capacity at ultrahigh rate via tunable surface pseudocapacitance, Adv. Mater. (2018).

[24] C. Guan, X. Li, Z. Wang, X. Cao, C. Soci, H. Zhang, H.J. Fan, Nanoporous walls on macroporous foam: rational design of electrodes to push areal pseudocapacitance, Adv. Mater. 24 (2012) 4186–4190.

[25] G. Xiong, P. He, D. Wang, Q. Zhang, T. Chen, T.S. Fisher, Hierarchical Ni-Co hydroxide petals on mechanically robust graphene petal foam for high-energy asymmetric supercapacitors, Adv. Funct. Mater. 26 (2016) 5460–5470.

[26] C. Yuan, J. Li, L. Hou, X. Zhang, L. Shen, X.W.D. Lou, Ultrathin mesoporous NiCo$_2$O$_4$ nanosheets supported on Ni foam as advanced electrodes for supercapacitors, Adv. Funct. Mater. 22 (2012) 4592–4597.

[27] W. He, C. Wang, H. Li, X. Deng, X. Xu, T. Zhai, Ultrathin and porous Ni$_3$S$_2$/CoNi$_2$S$_4$ 3D-network structure for superhigh energy density asymmetric supercapacitors, Adv. Energy Mater. 7 (2017) 1700983.

[28] F. Wang, X. Wu, X. Yuan, Z. Liu, Y. Zhang, L. Fu, Y. Zhu, Q. Zhou, Y. Wu, W. Huang, Latest advances in supercapacitors: from new electrode materials to novel device designs, Chem. Soc. Rev. 46 (2017) 6816–6854.

[29] S. Li, C. Yu, J. Yang, C. Zhao, M. Zhang, H. Huang, Z. Liu, W. Guo, J. Qiu, A superhydrophilic "nanoglue" for stabilizing metal hydroxides onto carbon materials for high-energy and ultralong-life asymmetric supercapacitors, Energy Environ. Sci. 10 (2017) 1958–1965.

[30] Y. Chen, W.K. Pang, H. Bai, T. Zhou, Y. Liu, S. Li, Z. Guo, Enhanced Structural STability of Nickel-cobalt Hydroxide Via Intrinsic Pillar Effect of Metaborate for High-power and Long-life Supercapacitor Electrodes, Nano Lett. 17 (2017) 429–436.

[31] W. Zhou, X. Cao, Z. Zeng, W. Shi, Y. Zhu, Q. Yan, H. Liu, J. Wang, H. Zhang, One-step synthesis of Ni3S2nanorod@Ni(OH)2nanosheet core–shell nanostructures on a three-dimensional graphene network for high-performance supercapacitors, Energy Environ. Sci. 6 (2013) 2216–2221.

[32] C. Shang, S. Dong, S. Wang, D. Dongdong Xiao, P. Han, X. Wang, L. Gu, G. Cui, Coaxial NixCo2x(OH)6×/TiN nanotube arrays as supercapacitor electrodes, ACS Nano 7 (2013) 5430–5436.

[33] X. Xiong, D. Ding, D. Chen, G. Waller, Y. Bu, Z. Wang, M. Liu, Three-dimensional ultrathin Ni(OH)2 nanosheets grown on nickel foam for high-performance supercapacitors, Nano Energy 11 (2015) 154–161.

[34] Z. Yu, J. Thomas, Energy storing electrical cables: integrating energy storage and electrical conduction, Adv. Mater. 26 (2014) 4279–4285.

[35] X. Xia, J. Tu, Y. Zhang, J. Chen, X. Wang, C. Gu, C. Guan, J. Luo, H.J. Fan, Porous hydroxide nanosheets on preformed nanowires by electrodeposition: branched nanoarrays for electrochemical energy storage, Chem. Mater. 24 (2012) 3793–3799.

[36] C. Cheng, H.J. Fan, Branched nanowires: synthesis and energy applications, Nano Today 7 (2012) 327–343.

[37] J. Zhao, J. Chen, S. Xu, M. Shao, Q. Zhang, F. Wei, J. Ma, M. Wei, D.G. Evans, X. Duan, Hierarchical NiMn layered double hydroxide/carbon nanotubes architecture with superb energy density for flexible supercapacitors, Adv. Funct. Mater. 24 (2014) 2938–2946.

[38] X. Xia, J. Tu, Y. Zhang, X. Wang, C. Gu, X. Zhao, H.J. Fan, High-quality metal oxide core/shell nanowire arrays on conductive substrates for electrochemical energy storage, ACS Nano 6 (2012) 5531–5538.

[39] C. Zhou, Y. Zhang, Y. Li, J. Liu, Construction of high-capacitance 3D CoO@ polypyrrole nanowire array electrode for aqueous asymmetric supercapacitor, Nano Lett. 13 (2013) 2078–2085.

[40] C. Guan, J. Liu, C. Cheng, H. Li, X. Li, W. Zhou, H. Zhang, H.J. Fan, Hybrid structure of cobalt monoxide nanowire @ nickel hydroxidenitrate nanoflake aligned on nickel foam for high-rate supercapacitor, Energy Environ. Sci. 4 (2011) 4496.

[41] S. Yang, C. Wu, J. Cai, Y. Zhu, H. Zhang, Y. Lu, K. Zhang, Seed-assisted smart construction of high mass loading Ni–Co–Mn hydroxide nanoflakes for supercapacitor applications, J. Mater. Chem. A 5 (2017) 16776–16785.

[42] H. Li, Y. Gao, C. Wang, G. Yang, A simple electrochemical route to access amorphous mixed-metal hydroxides for supercapacitor electrode materials, Adv. Energy Mater. 5 (2015) 1401767.

[43] G. Xiong, P. He, L. Liu, T. Chen, T.S. Fisher, Plasma-grown graphene petals templating Ni–Co–Mn hydroxide nanoneedles for high-rate and long-cycle-life pseudocapacitive electrodes, J. Mater. Chem. A 3 (2015) 22940–22948.

[44] J. Yang, C. Yu, X. Fan, J. Qiu, 3D architecture materials made of NiCoAl-LDH nanoplates coupled with NiCo-carbonate hydroxide nanowires grown on flexible graphite paper for asymmetric supercapacitors, Adv. Energy Mater. 4 (2014) 1400761.

[45] J. Kang, A. Hirata, L. Chen, S. Zhu, T. Fujita, M. Chen, Extraordinary supercapacitor performance of a multicomponent and mixed-valence oxyhydroxide, Angew. Chem. 54 (2015) 8100–8104.

[46] F. Ning, M. Shao, C. Zhang, S. Xu, M. Wei, X. Duan, Co$_3$O$_4$@layered double hydroxide core/shell hierarchical nanowire arrays for enhanced supercapacitance performance, Nano Energy 7 (2014) 134–142.

[47] Z. Li, M. Shao, L. Zhou, R. Zhang, C. Zhang, J. Han, M. Wei, D.G. Evans, X. Duan, A flexible all-solid-state micro-supercapacitor based on hierarchical CuO@layered double hydroxide core–shell nanoarrays, Nano Energy 20 (2016) 294–304.

[48] J. Xiao, L. Wan, S. Yang, F. Xiao, S. Wang, Design hierarchical electrodes with highly conductive NiCo$_2$S$_4$ nanotube arrays grown on carbon fiber paper for high-performance pseudocapacitors, Nano Lett. 14 (2014) 831–838.

[49] Q. Zhang, W. Xu, J. Sun, Z. Pan, J. Zhao, X. Wang, J. Zhang, P. Man, J. Guo, Z. Zhou, B. He, Z. Zhang, Q. Li, Y. Zhang, L. Xu, Y. Yao, Constructing ultrahigh-capacity zinc-nickel-cobalt oxide@Ni(OH)$_2$ core-shell nanowire arrays for high-performance coaxial fiber-shaped asymmetric supercapacitors, Nano Lett. 17 (2017) 7552–7560.

[50] Y. Lu, J. Nai, X.W.D. Lou, Formation of NiCo$_2$V$_2$ O$_8$ yolk-double shell spheres with enhanced lithium storage properties, Angew. Chem. 57 (2018) 2899–2903.

[51] Y. Li, G. Wang, T. Wei, Z. Fan, P. Yan, Nitrogen and sulfur co-doped porous carbon nanosheets derived from willow catkin for supercapacitors, Nano Energy 19 (2016) 165–175.

[52] Y. Jiang, Y. Wu, Y. Chen, Z. Qi, J. Shi, L. Gu, Y. Yu, Design Nitrogen (N) and Sulfur (S) Co-Doped 3D graphene network architectures for high-performance sodium storage, Small 14 (2018).

[53] Q. Zhang, J. Wang, D. Xu, Z. Wang, X. Li, K. Zhang, Facile large-scale synthesis of vertically aligned CuO nanowires on nickel foam: growth mechanism and remarkable electrochemical performance, J. Mater. Chem. A 2 (2014) 3865.

[54] Q. Zhang, K. Zhang, D. Xu, G. Yang, H. Huang, F. Nie, C. Liu, S. Yang, CuO nanostructures: synthesis, characterization, growth mechanisms, fundamental properties, and applications, Prog. Mater. Sci. 60 (2014) 208–337.

[55] Q. Zhang, H. Chen, L. Luo, B. Zhao, H. Luo, X. Han, J. Wang, C. Wang, Y. Yang, T. Zhu, M. Liu, Harnessing the concurrent reaction dynamics in active Si and Ge to achieve high performance lithium-ion batteries, Energy Environ. Sci. 11 (2018) 669–681.

[56] S. Xiong, J.S. Chen, X.W. Lou, H.C. Zeng, Mesoporous Co$_3$O$_4$and CoO@C topotactically transformed from chrysanthemum-like Co(CO$_3$)$_{0.5}$(OH)·0.11H$_2$O and their lithium-storage properties, Adv. Funct. Mater. 22 (2012) 861–871.

[57] X. Liu, Z. Chang, L. Luo, T. Xu, X. Lei, J. Liu, X. Sun, Hierarchical Zn$_x$Co$_{3-x}$O$_4$ nanoarrays with high activity for electrocatalytic oxygen evolution, Chem. Mater. 26 (2014) 1889–1895.

[58] J. Yang, C. Yu, X. Fan, C. Zhao, J. Qiu, Ultrafast self-assembly of graphene oxide-induced monolithic nico-carbonate hydroxide nanowire architectures with a superior volumetric capacitance for supercapacitors, Adv. Funct. Mater. 25 (2015) 2109–2116.

[59] X. Zou, A. Goswami, T. Asefa, Efficient noble metal-free (electro)catalysis of water and alcohol oxidations by zinc-cobalt layered double hydroxide, J. Am. Chem. Soc. 135 (2013) 17242–17245.

[60] X. Zhang, J. Zhang, K. Wang, Codoping-induced, rhombus-shaped Co3O4 nanosheets as an active electrode material for oxygen evolution, ACS Appl. Mater. Interfaces 7 (2015) 21745–21750.

[61] S. Niu, R. McFeron, F. Godínez-Salomón, B.S. Chapman, C.A. Damin, J.B. Tracy, V. Augustyn, C.P. Rhodes, Enhanced electrochemical lithium-ion charge storage of iron oxide nanosheets, Chem. Mater. 29 (2017) 7794–7807.

[62] V. Augustyn, E.R. White, J. Ko, G. Grüner, B.C. Regan, B. Dunn, Lithium-ion storage properties of titanium oxide nanosheets, Mater. Horiz. 1 (2014) 219–223.

[63] G.A. Muller, J.B. Cook, H.S. Kim, S.H. Tolbert, B. Dunn, High performance pseudocapacitor based on 2D layered metal chalcogenide nanocrystals, Nano Lett. 15 (2015) 1911–1917.

[64] B. Zhao, Z. Shao, From paper to paper-like hierarchical anatase TiO$_2$ film electrode for high-performance lithium-ion batteries, J. Phys. Chem. C 116 (2012) 17440–17447.

[65] L. Huang, D. Chen, Y. Ding, S. Feng, Z.L. Wang, M. Liu, Nickel-cobalt hydroxide nanosheets coated on NiCo2O4 nanowires grown on carbon fiber paper for high-performance pseudocapacitors, Nano Lett. 13 (2013) 3135–3139.

[66] J. Xiao, S. Yang, Sequential crystallization of sea urchin-like bimetallic (Ni, Co)

carbonate hydroxide and its morphology conserved conversion to porous $NiCo_2O_4$ spinel for pseudocapacitors, RSC Adv. 1 (2011) 588.

[67] H. Niu, X. Yang, H. Jiang, D. Zhou, X. Li, T. Zhang, J. Liu, Q. Wang, F. Qu, Hierarchical core–shell heterostructure of porous carbon nanofiber@$ZnCo_2O_4$ nanoneedle arrays: advanced binder-free electrodes for all-solid-state supercapacitors, J. Mater. Chem. A 3 (2015) 24082–24094.

[68] Z. Pan, Y. Jiang, P. Yang, Z. Wu, W. Tian, L. Liu, Y. Song, Q. Gu, D. Sun, L. Hu, In situ growth of layered bimetallic ZnCo hydroxide nanosheets for high-performance all-solid-state pseudocapacitor, ACS Nano 12 (2018) 2968–2979.

[69] B. Zhao, D. Chen, X. Xiong, B. Song, R. Hu, Q. Zhang, B.H. Rainwater, G.H. Waller, D. Zhen, Y. Ding, Y. Chen, C. Qu, D. Dang, C.-P. Wong, M. Liu, A high-energy, long cycle-life hybrid supercapacitor based on graphene composite electrodes, Energy Storage Mater. 7 (2017) 32–39.

[70] L. Qu, Y. Zhao, A.M. Khan, C. Han, K.M. Hercule, M. Yan, X. Liu, W. Chen, D. Wang, Z. Cai, W. Xu, K. Zhao, X. Zheng, L. Mai, Interwoven three-dimensional architecture of cobalt oxide nanobrush-graphene@$Ni_xCo_{2x}(OH)_{6x}$ for high-performance supercapacitors, Nano Lett. 15 (2015) 2037–2044.

[71] X. Wu, L. Jiang, C. Long, T. Wei, Z. Fan, Dual support system ensuring porous Co-Al hydroxide nanosheets with ultrahigh rate performance and high energy density for supercapacitors, Adv. Funct. Mater. 25 (2015) 1648–1655.

[72] J. Lin, H. Jia, H. Liang, S. Chen, Y. Cai, J. Qi, C. Qu, J. Cao, W. Fei, J. Feng, In situ synthesis of vertical standing nanosized NiO encapsulated in graphene as electrodes for high-performance supercapacitors, Adv. Sci. (2017) 1700687.

[73] L. Shen, J. Wang, G. Xu, H. Li, H. Dou, X. Zhang, $NiCo_2S_4$ nanosheets grown on nitrogen-doped carbon foams as an advanced electrode for supercapacitors, Adv. Energy Mater. 5 (2015) 1400977.

[74] L. Shen, L. Yu, H.B. Wu, X.Y. Yu, X. Zhang, X.W. Lou, Formation of nickel cobalt sulfide ball-in-ball hollow spheres with enhanced electrochemical pseudocapacitive properties, Nat. Commun. 6 (2015) 6694.

[75] Y. Bai, W. Wang, R. Wang, J. Sun, L. Gao, Controllable synthesis of 3D binary nickel–cobalt hydroxide/graphene/nickel foam as a binder-free electrode for high-performance supercapacitors, J. Mater. Chem. A 3 (2015) 12530–12538.

[76] X. Yu, B. Lu, Z. Xu, Super long-life supercapacitors based on the construction of nanohoneycomb-like strongly coupled $CoMoO_4$-3D graphene hybrid electrodes, Adv. Mater. 26 (2014) 1044–1051.

[77] C. Guan, X. Liu, W. Ren, X. Li, C. Cheng, J. Wang, Rational design of metal-organic framework derived hollow $NiCo_2O_4$ arrays for flexible supercapacitor and electrocatalysis, Adv. Energy Mater. 7 (2017) 1602391.

[78] S.Y. Kim, H.M. Jeong, J.H. Kwon, I.W. Ock, W.H. Suh, G.D. Stucky, J.K. Kang, Nickel oxide encapsulated nitrogen-rich carbon hollow spheres with multiporosity for high-performance pseudocapacitors having extremely robust cycle life, Energy Environ. Sci. 8 (2015) 188–194.

[79] S. Gao, Y. Sun, F. Lei, L. Liang, J. Liu, W. Bi, B. Pan, Y. Xie, Ultrahigh energy density realized by a single-layer beta-$Co(OH)_2$ all-solid-state asymmetric supercapacitor, Angew. Chem. 53 (2014) 12789–12793.

[80] T. Zhai, L. Wan, S. Sun, Q. Chen, J. Sun, Q. Xia, H. Xia, Phosphate ion functionalized Co_3O_4 ultrathin nanosheets with greatly improved surface reactivity for high performance pseudocapacitors, Adv. Mater. 29 (2017).

[81] T. Brousse, D. Belanger, J.W. Long, To be or not to be pseudocapacitive?, J. Electrochem. Soc. 162 (2015) A5185–A5189.

[82] K.A. Owusu, L. Qu, J. Li, Z. Wang, K. Zhao, C. Yang, K.M. Hercule, C. Lin, C. Shi, Q. Wei, L. Zhou, L. Mai, Low-crystalline iron oxide hydroxide nanoparticle anode for high-performance supercapacitors, Nat. Commun. 8 (2017) 14264.

[83] B. Delley, An all-electron numerical method for solving the local density functional for polyatomic molecules, J. Chem. Phys. 92 (1990) 508–517.

[84] J.P. Perdew, J.A. Chevary, S.H. Vosko, K.A. Jackson, M.R. Pederson, D.J. Singh, C. Fiolhais, Erratum: atoms, molecules, solids, and surfaces: applications of the generalized gradient approximation for exchange and correlation, Phys. Rev. B 48 (1993) 4978 (4978).

[85] S.J. Clark, M.D. Segall, C.J. Pickard, P.J. Hasnip, M.I.J. Probert, K. Refson, M.C. Payne, First principles methods using CASTEP, Z. Krist. 220 (2005) 567.